A model for oceanic melt rates under ice shelves using a balance-flux approach (CHICO)

D. Pollard[1] and R. M. DeConto[2]

[1]Earth and Environmental Systems Institute, Pennsylvania State University, University Park, PA 16802, USA

[2]Department of Geosciences, University of Massachusetts, Amherst, MA 01003, USA

Corresponding author: David Pollard (dxp21@psu.edu)

Key Points:

- A two-layer model of thermohaline ocean flow under ice shelves is described, and applied to Antarctica.
- It builds on previous models to simulate oceanic melt rates at the ice-shelf base, for use with ice-sheet models.
- A balance-flux approach is used, avoiding the need to pre-define geographical basin boundaries.

Abstract

A two-layer model of thermohaline ocean circulation under Antarctic ice shelves is described that predicts sub-oceanic ice-shelf melt rates given the basin geometries and ocean temperatures and salinities at the ice edges. The model builds on a series of similar models, using an upper plume layer and adding a balance-flux approach that enables it to be used for evolving land-ocean geometries without the need to pre-define individual basin outlines. Results are compared to Antarctic melt rates derived from satellite data. The model is shown to work for two simulated configurations of West Antarctica very different from modern. In Supporting Information several alternate model aspects are described, and results are tested against numerical solutions of the basic plume differential equations for 1-D flowlines.

1 Introduction

Oceanic melting at the base of Antarctic ice shelves strongly influences their extent, thickness and buttressing of upstream ice, which is important for major glacier outlets currently undergoing thinning and retreat such as Pine Island and Thwaites Glaciers in the West Antarctic Amundsen Sea (ASE) region, and Totten and Denman Glaciers in East Antarctica (Jenkins et al., 2018; Roberts et al., 2018; Miles et al., 2020).

Rates of melt are determined by oceanic flow from the Southern Ocean across the continental shelves and under sub-ice-shelf cavities (Schmidtko et al., 2014; Tinto et al., 2019; Adusumilli et al., 2020; Stevens et al., 2020). Accurate simulation requires high-resolution regional ocean modeling extending under ice shelves (Hellmer et al., 2012; Dutrieux et al., 2014; Gwyther et al., 2014; Yokoyama et al., 2016; Richter et al., 2020; reviewed in Dinniman et al., 2016; Asay-Davis et al., 2017), which is computationally expensive and has not yet been used in coupled ice-ocean studies on long-term continental scales to our knowledge.

In the interim, a series of simpler models building on each other have been applied to the oceanic flow in the cavity between the ice-shelf edge and the grounding line (Olbers and Hellmer, 2010; Lazeroms et al., 2018 (henceforth LAZ); Reese et al., 2018 (PICO), Pelle et al, 2019, 2020 (PICOP)). These models are designed to efficiently provide ice-sheet models with oceanic melt rates, given ocean temperatures and salinities outside the shelves. Ocean dynamics are simplified as a thermohaline convective overturning cell, with prescribed incoming ocean water at depth from the cavity edge to the grounding line, and outgoing flow in contact with the ice base from the grounding line to the edge. Results have been compared with observationally deduced ocean melt rates for the ~20 largest ice shelves around Antarctica (Rignot et al., 2013; Adusumelli et al., 2020; cf. Moholdt et al., 2014; Gwyther et al., 2014; Shean et al., 2019).

In the LAZ, PICO, and PICOP models, the ice-shelf cavity dynamics have essentially one horizontal dimension running from the edge of the ice shelf to the inner grounding line. The second horizontal dimension is either collapsed to a transverse average (PICO), or based on proximal grounding-line depths or basal ice slopes for the upper plume (LAZ, PICOP). This has two drawbacks that we attempt to improve on here: (i) it does not account for horizontal convergence or divergence of flow, and (ii) for PICO and PICOP, it requires individual ice-shelf basins to be pre-defined based on the modern configuration, over which transverse averages are applied (Reese et al., 2018).

The second of these is problematic for modeling long-term Antarctic evolution involving collapse and regrowth of the West Antarctic Ice Sheet (WAIS). A fully collapsed WAIS with an interior ocean and separate land masses in the Peninsula and Marie Byrd Land, and regrowth with individual ice shelves expanding and coalescing from these land masses, can produce ice-shelf configurations topologically different from the present. An automatic algorithm that can sensibly define basin outlines for general grounding-line topologies may be possible, but after some effort we were unable to find a fully general working algorithm.

An alternate approach for the second horizontal dimension is provided by the balance-flux method, previously applied to ice-sheet modeling (Warner and Budd, 2000). For an equilibrated ice sheet, i.e., with negligible temporal changes in ice thickness, ice velocities between grid cells can be deduced from a given 2-D map of surface mass balance (snowfall minus melt), assuming only that flow directions must be down the surface slope, and given a parameterization partitioning the outgoing flow from a cell into the adjacent downhill cells if there are more than one. The cells are first sorted in order of decreasing surface elevation. Then if cell fluxes are calculated in that order, all incoming fluxes for a cell will have been determined before that cell is reached in the calculations, and its total outgoing flux is set to the sum of the incoming fluxes plus its surface mass balance.

This approach is used here in a new model (CHICO, CHild of pICO), with two layers: the lower layer with "inbound" flow from the oceanic shelf edges to the grounding lines, and the upper plume layer with "outbound" flow from grounding lines back to the oceanic edges. Similarly to PICO, a non-dimensional distance metric is defined, running from zero at shelf edges and increasing towards the innermost grounding lines, which replaces ice-sheet surface elevation in the balance-flux method. Balance-flux calculations are applied to both layers, first to the inbound lower layer from the edges to grounding lines, and then to outbound upper layer in reverse order, from the grounding lines to the edges. The balance fluxes also advect temperature and salinity conserving heat and mass (and momentum for the upper layer), and oceanic melt rates at the ice base are calculated as part of the upper-layer calculations, as in the earlier models. The balance-flux approach accounts for horizontal convergence or divergence in each layer, and can be applied over the whole domain for an arbitrary configuration of grounding-line patterns and ice-shelf extents.

In common with the previous models, this approach cannot capture aspects of the real 2-D and 3-D sub-ice ocean circulation due to Coriolis acceleration, tidal mixing and other dynamics. Also there is no influx of sub-glacial discharge at grounding lines (e.g., Dow et al., 2020). Except for the balance-flux approach that avoids the need to specify basin boundaries, no fundamental additional physics are added beyond that in the LAZ/PICO/PICOP models.

The model formulation is described in section 2. In section 3 computed modern melt rates are shown for Antarctic regions and ice shelves at different resolutions, driven by climatological ocean temperatures and salinities at the shelf edges, and compared to observationally deduced melt rates. Parameter values are selected from a large ensemble of runs, with scoring based on observed average melt rates for individual ice shelves. Also in section 3 two examples are shown from previous long-term simulations with collapsed WAIS, to show that the approach works for land-ocean-shelf configurations very different from modern. In Supporting Information (SI) section 1, modern results are contrasted with a much simpler ocean-melt parameterization used in previous long-term ice-sheet modeling. SI section 2 shows results using an alternate form of the non-dimensional distance metric as used in PICO and PICOP, SI section 3 shows several other plume variables to illustrate model performance, and SI section 4 describes an option to include additional seasonal melting near the ice edge. In SI section 5, results are tested against numerical solutions of the basic differential equations for plume flow in 1-D flowline settings.

2. Model formulation

As shown in Fig. 1, the model has two layers, similarly to LAZ, PICO and PICOP. The lower layer represents inflow from the open ocean adjacent to the ice shelf edge to the grounding line. In the previous models it is assumed to be uniform with temperature and salinity equal to the outer ocean water (which may be regarded as prescribed inputs and not a model layer). Here the lower layer is modeled as spatially varying within the balance-flux framework, to accommodate incoming oceanic temperatures and salinities that may vary along the ice-shelf edge and merge under the ice shelf (thus avoiding having to average them along the edges of pre-defined basins). The upper layer represents outflow from the grounding line back to the ice-shelf edge, and uses 1-D plume dynamical equations (Lazeroms et al., 2018) as in LAZ and PICOP.

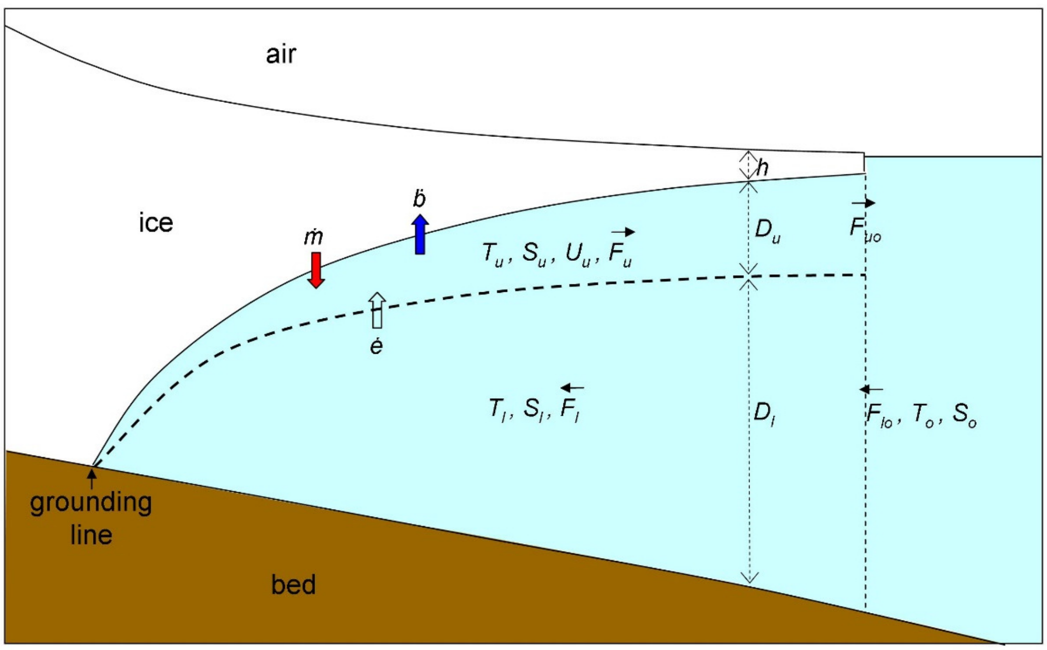

Figure 1. Schematic picture of the two-layer model. Subscripts l and u here are for the lower and upper layer respectively; u is omitted for simplicity in the text. T_l, S_l, F_l, D_l are temperature, salinity, horizontal mass flux and thickness of the lower layer, respectively, and T_u, S_u, F_u, D_u are the same for the upper layer. U_u is upper-layer horizontal velocity. $\dot{m}$ and $\dot{b}$ are melt and freeze-on rates respectively at the base of the ice shelf, and h is ice-shelf thickness. $\dot{e}$ is the turbulent entrainment rate of lower-layer water into the upper layer. T_o and S_o are prescribed temperature and salinity of inflowing ocean water into the lower layer at the ice-shelf edge, with incoming mass flux F_{lo}. The return mass flux from upper layer to the ocean is F_{uo}, = F_u at the ice-shelf edge.

2.1. Physical equations

The conservation equations for the upper plume layer (Jenkins, 1991, 2011; Lazeroms et al., 2018) are

$$\frac{\partial D}{\partial t} + \frac{\partial DU}{\partial x} = \dot{e} + \dot{m} \tag{1a}$$

$$\frac{\partial DU}{\partial t} + \frac{\partial DU^2}{\partial x} = D\frac{\Delta\rho}{\rho_o} g \sin\alpha - C_d U^2 \tag{1b}$$

$$\frac{\partial DT}{\partial t} + \frac{\partial DUT}{\partial x} = \dot{e}T_l + \dot{m}\,T_f + C_d^{1/2}\Gamma_T\, U\big(T_f - T\big)\, f_e \tag{1c}$$

$$\frac{\partial DS}{\partial t} + \frac{\partial DUS}{\partial x} = \dot{e}S_l \tag{1d}$$

where x is distance along flow, and D, U, T and S are layer thickness (m), horizontal velocity (m s^{-1}), temperature (°C) and salinity (permil, ‰) of the upper layer. D_l, T_l, and S_l are the same quantities for the lower layer; for clarity a subscript is not generally used for the upper layer. $\Delta\rho$ is lower minus upper-layer density, and ρ_0 = 1033 kg m^{-3}. g = 9.81 m s^{-2} is gravitational acceleration, and α is the slope of the ice-shelf base in the outward direction. C_d is a drag coefficient = 3 x 10^{-3}, and $C_d^{1/2}\ \Gamma_T$ is a turbulent heat exchange coefficient with Γ_T = 3 x 10^{-2}. In Eq. (1d) the salinity of melted ice is assumed to be zero. Ocean water densities used to compute $\Delta\rho$ depend linearly on temperature and salinity as in Reese et al. (2018):

$$\rho = \rho_o\big(1 - \beta_T(T - T_r) + \beta_S(S - S_r)\big)$$

where β_T= 7.5 x 10^{-5} °C^{-1}, T_r = 0 °C, β_S = 7.7e-4 ‰$^{-1}$ and S_r = 34 ‰.

$\dot{e}$ is the entrainment rate of lower-layer water in to the upper layer (m s^{-1} of ocean water equivalent), given as in Lazeroms et al. (2018) by

$$\dot{e} = E_o\, U \sin\alpha \tag{2}$$

where E_o = 1 x 10^{-2}. The values of C_d, Γ_T and E_o are set from an ensemble of model runs described in section 3.2.

$\dot{m}$ is the melt rate at the base of the ice shelf (m s^{-1}), given by an approximate simplification of the full 3-equation boundary-layer system as in Lazeroms et al. (2018) and Reese et al. (2018):

$$\dot{m} = \frac{c_w}{L}\, C_d^{1/2}\Gamma_T\ U\big(T - T_f\big)\, f_e \tag{3}$$

where c_w is the specific heat of ocean water (4218 J kg^{-1} C^{-1}), L is the latent heat of freezing (3.35 x 10^{-5} J kg^{-1}), and T_f (°C) is the freezing point of the plume water, depending linearly on salinity and depth as in Reese et al. (2018):

$$T_f = -\lambda_1 S + \lambda_2 - \lambda_3\, \rho_w g z$$

where λ_1 = 0.0572 °C ‰$^{-1}$, λ_2 = 0.0788 °C, and λ_3 = 7.77 x 10^{-8} °C Pa^{-1}. z is depth (m) below the ocean surface, related to ice-shelf thickness h by $z = (\rho_i/\rho_w)\, h$, where ρ_i = 910 kg m^{-3} and ρ_w =

1028 kg m^{-3} are ice and ocean water densities respectively. f_e is the fractional cover of ice shelf in each grid cell (= 1 except potentially at the edge); h and f_e are supplied by observations or by an ice-sheet model.

For the lower layer, Eqs. (1c) and (1d) are used for temperature and salinity T_l and S_l, with $\dot{e}$ replaced by -$\dot{e}$, and with no ice-base or ice-melting terms (K=0, $\dot{m}$=0). Lower-layer velocity U_l is not solved for explicitly (see below).

The time scales of ice-sheet applications are much longer than the circulation timescales in ice-shelf cavities, so the overturning flow described by Eqs. (1) is essentially equilibrated to the current geometry and exterior ocean properties, and all $\partial/\partial t$ terms in (1) can be neglected. They are used however to obtain flowline solutions of Eqs. (1) in SI section 5.

2.2 Finite-difference balance-flux form

In order to use the balance-flux approach, we discretize Eqs. (1) as follows, similarly to Reese et al. (2018) and sketched in Fig. 2. The following applies to the upper layer, but is also used for the lower layer with momentum and melting omitted.

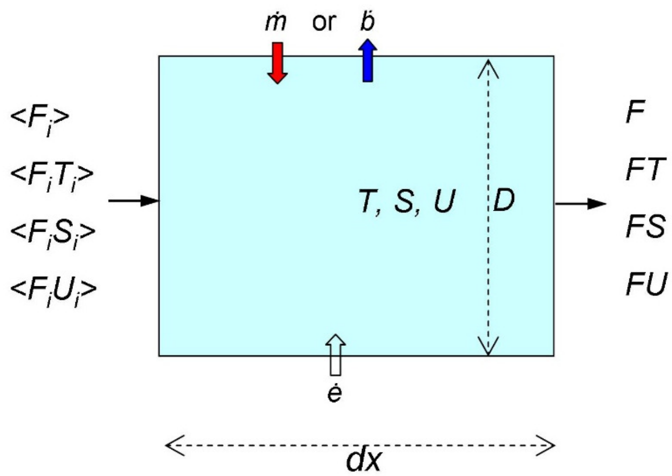

Figure 2. Schematic discretization for one grid cell of the upper layer in solving Eqs. (4). Flow is left to right. D, U, T, and S are layer thickness, velocity, temperature and salinity. $<F_i>$, $<F_iU_i>$, $<F_iT_i>$ and $<F_iS_i>$ are the net incoming mass, momentum, heat and salt fluxes respectively from upstream neighboring cells, and F is the outgoing mass flux to downstream neighbors. $\dot{m}$, $\dot{b}$ and $\dot{e}$ are melt rate, freeze-on rate, and lower-layer entrainment rate, respectively. dx is the grid cell size in the along-flow direction.

$$F = \langle F_i \rangle + (\dot{e} + \dot{m})\, dx \tag{4a}$$

$$U[\langle F_i \rangle + (\dot{e} + \dot{m})\, dx + C_d U dx] = \langle F_i U_i \rangle + D \frac{\Delta\rho}{\rho_o} g \sin\alpha\, dx \tag{4b}$$

$$T[\langle F_i \rangle + (\dot{e} + \dot{m})\, dx + K U f_e dx] = \langle F_i T_i \rangle + \left(\dot{e} T_l + \dot{m}\, T_f + C_d^{1/2} \Gamma_T\, U f_e T_f\right) dx \tag{4c}$$

$$S[\langle F_i \rangle + (\dot{e} + \dot{m})\, dx] = \langle F_i S_i \rangle + \dot{e} S_l dx \tag{4d}$$

$$F = D\,U \tag{5}$$

where F and F_i are mass fluxes (m^2 s^{-1}) per unit length in the transverse direction, and dx is the grid-cell dimension (m) in the along-flow direction. F is the total mass flux out of each cell, to be partitioned into all adjacent downstream cells. $<F_i>$ is the sum of incoming mass fluxes from adjacent upstream cells, $<F_iU_i>$ is the sum of the products of incoming fluxes and velocities of adjacent cells, and similarly for $<F_iT_i>$ and $<F_iS_i>$; these are all already known due to the sorted order of the balance-flux method.

"Upstream" and "downstream" in the balance-flux method are determined by the sign of gradients of the non-dimensional distance metric R (see below). Once Eqs. (4) are solved for a grid cell, the outgoing fluxes F, FT, FS and FU are partitioned into incoming fluxes for adjacent downstream cells (potentially in all 8 directions in our Cartesian grid). We tried two ways of partitioning: proportional to the magnitude of $\nabla(R)$, and equal weighting for all downstream neighbors. The second method yields better results, allowing greater lateral dispersion, and is used throughout here.

As described below, these equations are applied in two passes, first an incoming pass for the entire lower layer, and then an outgoing pass for the upper plume layer. For the lower layer, velocity U is not solved for (no Eq. 4b and does not appear in Eqs. 4a,c,d), $\dot{e}$ is replaced by $-\dot{e}$, and Γ_T and $\dot{m}$ are zero. This reflects the fact that the lower layer is simply filled by inflowing ocean water from the ice-shelf edge, with no vertical heat or salt exchange; (entrainment into the upper layer is a mass loss but does not locally change the lower-layer temperature or salinity). The only purpose of the lower-layer equations is to spatially merge ocean properties from around the edge as the water flows into the lower layer.

Note that with the balance-flux method, there is no need to complete calculations of individual ice shelves before moving on to the next one; the only requirement is to perform the calculations for each grid cell in the appropriate order of the distance metric R for each pass (ascending for lower layer, descending for upper layer). The grid-cell calculations of Eqs. (4) can jump from basin to basin, until all grid cells containing ice shelves in the domain have been processed for each pass.

2.3 Solution for upper-layer velocity, and sub-iteration

Eqs. (4) are four algebraic equations for one cell's T, S, U and D (with F, $\dot{e}$, $\dot{m}$, $\Delta\rho$ and T_f given by Eqs. 2, 3, 5 and other relations above). Eqs. (4a) and (4b) are solved first for U and D. Re-arranging Eqs. (4a,b), and using (2), (3) and (5),

$$D\,U = E_o\,U \sin\alpha\,dx + \frac{c_w}{L}\,C_d^{1/2}\Gamma_T\;U\left(T - T_f\right) f_e + \langle F_i\rangle \tag{6a}$$

$$D\,U^2 = D\,\frac{\Delta\rho}{\rho_o} g \sin\alpha\,dx - C_d U^2 dx + \langle F_i U_i\rangle \tag{6b}$$

Eliminating D,

$$U^3(K\,dx + C_d dx) + U^2\left(\langle F_i\rangle\right) + U\left(-\langle F_iU_i\rangle - \frac{\Delta\rho}{\rho_o} g \sin\alpha\,K\,dx^2\right) - \left(\frac{\Delta\rho}{\rho_o} g \sin\alpha\,\langle F_i\rangle\,dx\right) = 0 \tag{7a}$$

where K is a combination of entrainment and melt terms

$$K = E_o \sin\alpha + \frac{c_w}{L} C_d^{1/2} \Gamma_T \left(T - T_f\right) f_e \tag{7b}$$

Eq. (7a) is a cubic for U that is solved by straightforward binary search (there is always just one positive real root, considering the signs of the coefficients). Then D is determined from (5), i.e., $D = F/U$ with F given by Eq. (4a). Finally Eqs. (4c) and (4d) are used with (2) and (3) to solve for T and S.

In Eq. (7a,b), temperature T, salinity S and hence T_f and $\Delta\rho$ are initially unknown. A sub-iteration over Eqs. (4a-d) and (7a,b) is performed using T, S, T_f and $\Delta\rho$ from the previous iteration where needed, to converge on consistent solutions for U, D, T and S. This sub-iteration converges well for most locations, but care is needed for low slopes (sin α) and thin layers (D) which tend to occur close to interior grounding lines of large basins. A simple damping (80%) of the changes in U, D, T and S at each iteration is needed in these cases.

As part of the sub-iteration, if the plume temperature T falls below the freezing point T_f, T is reset to T_f, $\dot{m}$ is set to zero, and some plume water is frozen on to the ice base, conserving the sum of sensible and latent heat. This occurs due to the "ice pump" mechanism as plume water is advected to shallower depths and so increasing T_f. In this case, the rate of freezing $\dot{b}$ (m s^{-1} of ocean water equivalent) is given by

$$\dot{b} = \frac{c_w}{L} \left(\lambda_3 \, \rho_w g \sin\alpha \, UD - E_o \sin\alpha \, U\left(T_l - T_f\right)\right) \tag{8}$$

where $\lambda_3 \rho_w g \sin \alpha$ is the rate of increase of T_f per unit distance in the flow direction due to the shallowing ice base, and the second term involving the lower-layer temperature T_l is partially compensating warming by entrainment. The effect of along-flow gradients of salinity S on T_f is neglected, as it is generally much smaller than the effect of basal slope. For ice-sheet model applications, $\dot{m} - \dot{b}$ would be returned as the net sub-ice oceanic forcing, and is shown as net melt in the figures below.

To improve numerical accuracy for coarser grid sizes, a slight modification to the finite differencing is made for upper-layer grid cells adjacent to a grounding line with no influx from adjacent cells. At the grounding-line interface of these cells, horizontal velocity is zero, and is assumed to increase linearly across the cell to the value U given by the solution above. Consequently the entrainment and melt coefficients E_o and $C_d^{1/2}\, \Gamma_T$ above are each multiplied by 1/2 to account for the average value of velocity across the cell, and the drag coefficient C_d is multiplied by 1/3 to account similarly for velocity squared.

2.4 Lower-layer and upper-layer passes, overturning strength

Two passes are performed with the above equations: first, for the lower layer, sweeping from the ice-shelf edges to grounding lines in balance-flux order. Then, the flow in the upper plume layer is calculated, sweeping in reverse balance-flux order from the grounding lines to the edges.

At the start of the lower-layer pass, values of incoming fluxes F_i, F_iT_i and F_iS_i need to be specified for cells at ice-shelf edges adjacent to open ocean. These mass fluxes F_i are set initially to an arbitrary value (F_{lo} = 0.5 m^2 s^{-1} per unit transverse length), and F_iT_i and F_iS_i are set to that value multiplied by the adjacent open-ocean temperature T_o and salinity S_o (see below). As the lower-layer water flows inward, some is lost to entrainment into the upper layer, but if not all lost, lower-layer cells adjacent to grounding lines may have incoming fluxes but no adjacent upstream cells to receive outgoing flux. The model has an option to supply this flux upwards to the co-located upper-layer cell, to initiate the next upper-layer pass. For the standard model we assume that this "reversal" of flow (lower-to-upper cell) at grounding lines is negligible, and initialize all incoming upper-layer fluxes at grounding-line cells to zero for the start of the upper-layer pass.

If "reversal" fluxes at grounding lines are included, outgoing fluxes are increased in the upper layer. However, this does not lead to a physically meaningful strength of the overall thermohaline circulation, because water mass is conserved in the model and the net outflow to the ocean is the same as the arbitrarily prescribed inflow (an average of 0.5 m^2 s^{-1} per transverse length) plus ice melt. The magnitudes of real-world cavity-ocean exchange rates are poorly known, and their parameterization would involve the energetics of the whole cavity overturning including bottom drag (cf. coefficient C in Reese et al., 2018, and discussed further in Olbers and Hellmer, 2010).

By setting "reversal" fluxes to zero, the standard model in effect assumes that the energetics controlling the cavity overturning strength are captured explicitly in the upper-layer dynamical equations Eqs. (1b) and (4b), with acceleration due to buoyancy balanced by frictional drag. The net outgoing upper-layer flux to the ocean at shelf edges (F_{uo}, = F in Eq. 4a for the edge cells) is then meaningful as the overall strength and is given in Table 1 below. The incoming lower-layer flux from the ocean (F_{lo}) should exactly balance total entrainment ($\dot{e}$) into the upper layer on a basin by basin basis.

To accomplish the latter it may seem logical to perform an iteration over pairs of passes, in which the lower-layer inflow F_{lo} at shelf edges is set equal to the upper-layer outflow F_{uo} of the previous iteration (actually at each co-located point, which accomplishes the same for each basin, neglecting ice melt). However the value(s) for incoming F_{lo} at shelf edges makes very little difference in the standard model, because the only physics involved in the lower layer is the filling of its volume with ocean water as discussed in section 2.2. It has no effect at all if ocean properties T_o and S_o are uniform around the ice-shelf edges, as the lower layer then fills uniformly with $T_l = T_o$ and $S_l = S_o$. If not uniform, the only effect is to slightly influence their advection across the lower layer due to iteratively changing detrainment $-\dot{e}$ into the upper layer. Here we do perform two iterations in this way (with $F_{lo} = 0.5$ m^2 s^{-1} and $-\dot{e} = 0$ for the first lower-layer pass, and using $-\dot{e}$ from the first upper-layer pass for the second lower-layer pass), but the effect on the results compared to a single pair of passes is very small.

2.5 Plume termination

In the above solutions, if the density difference $\Delta\rho \leq 0$, upper-layer velocity $U \leq 0$, or thickness $D \leq D_{min}$, the upper-layer plume is assumed to terminate or cannot originate (as mentioned in Jenkins, 1991, 2011). The minimum thickness $D_{min} = 0.5$ $(dx/10^4)$ meters is dependent on grid size dx (m) to permit slowly thickening plume layers to emerge from grounding lines with nearly flat basal ice slopes. The resulting behavior is beyond the scope of the model, but presumably there is considerable vertical mixing with the lower layer. Where termination occurs we simply reset upper-layer temperature and salinity T, S to the local lower-layer values T_l, S_l, reset thickness D to 2 D_{min}, and maintain upper-layer mass flux at its incoming value. Plume flow can resume downstream if $\Delta\rho$ becomes positive. Plume termination happens rarely in the model, mostly at single grid cells along limited portions of grounding lines (and the plume originates in the next grid cell away from the grounding line).

2.6 Non-dimensional distance metric *R*

A non-dimensional distance metric is defined to control the order of the balance-flux calculations, corresponding to ice surface elevation in ice-sheet applications. The direction of horizontal flux between adjacent grid cells is determined by the slope of R, and is the same but opposite for the upper lower and upper layer. It is meant to represent the directions of the real overturning circulation between ice-shelf edges and grounding lines.

First, quantities d_e and d_g are calculated for each grid cell, the distances to the closest ice-shelf edge with open ocean (d_e) and to the closest grounding line (d_g). An incremental-neighbor calculation is used for each. For d_e, the calculation starts by setting $d_e = 0$ for all ice-shelf edge points adjacent to open ocean. d_e is then set for all neighboring points containing floating ice (including diagonal neighbors), incrementing d_e by the center-to-center distance between points. This procedure is applied iteratively until all points with floating ice have been reached. This results in the shortest path to the ice-shelf edge, staying within the ice shelf and going around interior grounded islands. Exactly the same procedure is used for d_g, starting with $d_g = 0$ at all ice-shelf "grounding-line" points contiguous to the grounding ice, and incrementally expanding to ice-shelf edges. For these calculations, any polynyas are considered to contain floating ice, which avoids spurious R gradients that would occur if polynyas were considered open-ocean or grounded regions.

For most simulations in the paper, the non-dimensional distance metric R is simply

$$R = d_e/d_0 \tag{9}$$

$d_0 = 1000 \times 10^3$ m is an arbitrary normalizing scale, used for convenience to make $R \sim O(1)$ for large shelves, but has no influence on the results. R increases from 0 at all ice-shelf edges, to larger values deeper into the basin. Its value is not constant around grounding lines. An alternate form of R is described in SI section 2.

An important goal in the definition of R is to yield broad-scale smooth patterns of ocean flow from the shelf edges through the shelf interior to the inner grounding lines (for the lower layer, and vice versa for the upper layer), without introducing spurious smaller-scale non-physical flow features. This goal is partially met by Eq. (9), but for that, some spatial smoothing needs to be applied. If this is not done, smaller-scale irregularities in the grounding-line edges of large shelves such as the Ross and Filchner-Ronne produce ridges and valleys in R extending some way into the shelf interior, funneling balance fluxes into narrow channels through some of the shelf. This smoothing is done simply by linear diffusion of R, maintaining $R = 0$ at ice-shelf edges. The amount of diffusion is equivalent to integrating

$$\frac{\partial R}{\partial t} = D_d \left(\frac{\partial^2 R}{\partial x^2} + \frac{\partial^2 R}{\partial y^2} \right) \tag{10}$$

where $D_d = 10^8$ m^2 yr^{-1}, applied for a duration $\tau_R = 10$ years. This smooths most of the wiggles emanating from the major shelf edges, but preserves the overall gradient in R from outer edges to inner grounding lines, as shown in SI section 2. The length scale below (above) which fluctuations are effectively smoothed (preserved) is $(D_d\ \tau_R)^{1/2} \approx 30$ km.

After smoothing, isolated "depressions" where R has a local minimum are filled in. Because of the overall gradient of R from outer edge to inner grounding lines, these are rare and limited to just a few points. If not filled in, the balance fluxes on the inward lower-layer pass (upgradient of R) would not reach these depressions and the whole calculation would fail. This infilling is exactly equivalent to the well-known depression-filling problem in hydrology for which relatively sophisticated algorithms have been developed (e.g., Huang and Lee, 2015). But because these regions are rare and isolated, we use a much simpler method by simply increasing R at single points with a local minimum to the smallest value of its neighbors + .0001. This is iterated over the whole domain until all such points are eliminated.

2.7 Smoothing of sin α

A small amount of spatial smoothing is also applied to sin α used in Eqs. (2), (4b) and (7). sin α is the gradient $\partial z/\partial x$ of the ice-shelf base in the direction of ∇R, with $z = (\rho_i/\rho_w)h$ and ice thickness h supplied from observations or an ice-sheet model. α can be noisy on the scale of a few grid cells and can spuriously disrupt the results (see SI section 5). Simple linear diffusion is applied as for R above, with the same coefficient $D_d = 10^8$ m^2 yr^{-1} but for a duration $\tau_\alpha = 0.1$ years, so the length scale of effective smoothing $(D_d\ \tau_\alpha)^{1/2} \approx 7$ km. The duration τ_α is varied in the model ensemble described below.

$$\frac{\partial(\sin a)}{\partial t} = D_d\left(\frac{\partial^2(\sin a)}{\partial x^2} + \frac{\partial^2(\sin a)}{\partial y^2}\right) \tag{11}$$

2.8 Prescription of oceanic temperature and salinity

Oceanic temperature and salinity (T_o and S_o) need to be prescribed for incoming fluxes at ice shelf edges for the lower layer. Here these are derived from the World Ocean Atlas 2018 database (Boyer et al., 2018; henceforth WOA), then modified at ice-shelf edges as described below. Several distinct water masses have been identified: High Salinity Shelf Water (HSSW) Circumpolar Deep Water (CDW); and Antarctic Surface Water (AASW) (Schmidtko et al., 2014; Tinto et al., 2019; Adusumilli et al., 2020; Stevens et al., 2020). Following Adusumilli et al. (2020), at each WOA grid location we take the maximum annual mean temperature of all layers between 200 and 800 m depths; this roughly represents a combination of HSSW and CDW waters (Mode 1 and Mode 2 melting respectively) and avoids shallow seasonal AASW water (Mode 3 melting; cf. SI section 4). The same layer is also used for annual mean WOA salinity.

The decadal average (1981-2010) WOA fields of T_o and S_o are then interpolated from the one-degree longitude-latitude WOA grid to the ice-sheet grid, and then extrapolated (by iterative nearest-neighbor assignment like that used in the calculation of d_e and d_g above) into oceanic regions adjacent to ice shelves. In some regions, the distance of this extrapolation can be considerable, and can produce spurious sharp quasi-discontinuities in T_o and S_o near the ice-shelf edges. To reduce these spurious features, linear diffusion as in Eq (11) is applied to T_o and S_o, only in the regions where they are extrapolated beyond the database coverage, with the same coefficient $D_d = 10^8$ m^2 yr^{-1} for a duration $\tau_o = 25$ years, so the length scale of effective smoothing $(D_d\ \tau_o)^{1/2} \approx 50$ km.

After these operations, our distribution of oceanic temperatures T_o around ice-shelf edges resemble those in Adusumilli et al. (2020, their Fig. 1, noting their values are relative to the freezing point). However, the average values of T_o for individual ice shelves were significantly different from many of those in Reese et al. (2018, their Table 2), who used circum-Antarctic oceanic data in Schmidtko et al. (2014) to force the PICO model. The most serious differences were in the Amundsen Sea, where our T_o values for Thwaites and Pine Island shelf edges were ~2 ^{o}C colder than theirs, and for many East Antarctic shelves our T_o were ~1 ^{o}C warmer. In initial attempts to find best-fit parameters in our model ensembles (see below), this led to an inability to yield realistically high melt rates for Amundsen Sea shelves while keeping East Antarctic melt rates reasonably low. For the purposes of robust model evaluation and more direct comparisons with previous models (LAZ/PICO/PICOP), we therefore apply a uniform shift to T_o and S_o around each individual ice-shelf edge, to make the average for each shelf equal to those in Reese et al. (2018)'s Table 2 (while preserving the intra-shelf spatial variations from the WOA data). The resulting average values are shown in Table 1.

3. Results

3.1 Modern Antarctica

The model is applied to modern Antarctica, with ice and bedrock states prescribed from the Bedmachine dataset (Morlighem, 2020; Morlighem et al., 2020) aggregated to the model polar stereographic grid. The WOA 2018 climatological dataset (Boyer et al., 2018) is used to prescribe open-ocean temperature and salinities, using appropriate depths, extrapolated to the ice-shelf edges, and shifted to agree with Reese et al. (2018) as described above. Modern sub-ice ocean melt rates derived using satellite data on ice surface heights and velocities are taken from the dataset of Adusumilli et al. (2020). In addition to spatial maps of ocean melt, results are analyzed for individual ice shelves using the same set as in Reese et al. (2018) with locations shown in Fig. 3.

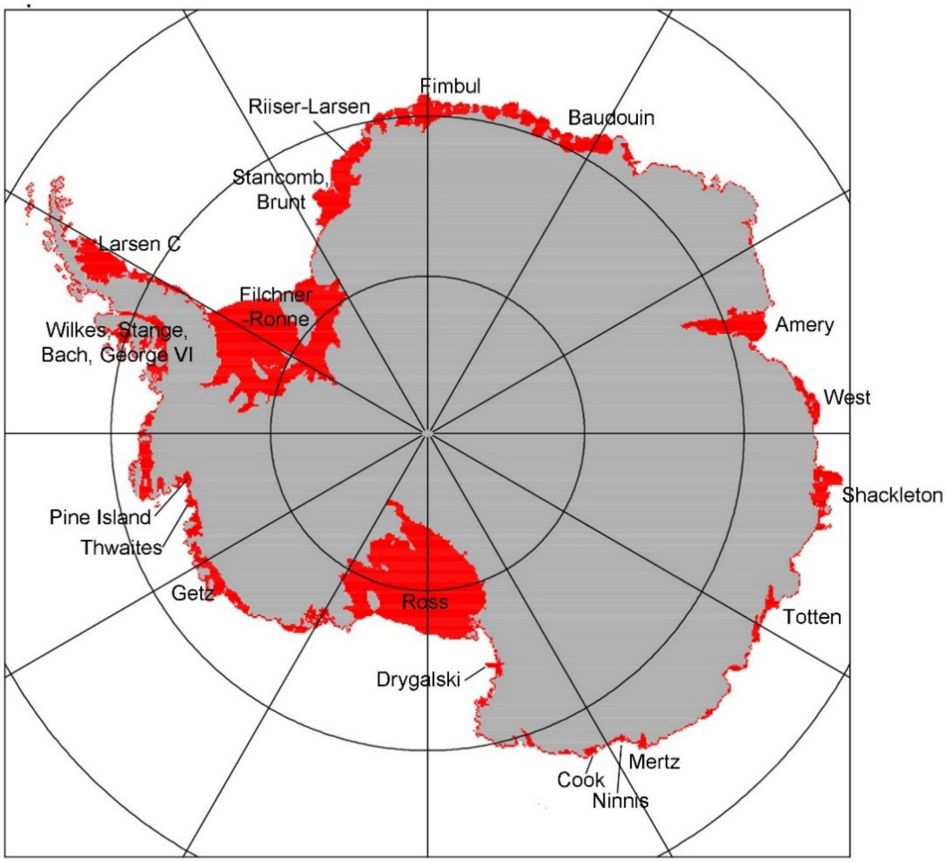

Figure 3. Location map of the Antarctic ice shelves used for modern comparisons (same as in in Reese et al., 2018). Ice-shelf extents are regridded to our 10-km grid from the Bedmachine dataset (Morlighem, 2020; Morlighem et al., 2020) and shown in red.

Fig. 4 shows model ocean melt rates (upper row) compared to observed (bottom row), for three different domains and grid resolutions: all Antarctica at 10 km, West Antarctica at 5 km, and the eastern Amundsen Sea Embayment at 2 km. The 10-km scale is typical of long-term continental ice-sheet modeling applications, and is tested here even though it does not properly resolve some small ice shelves. At the continental scale, the magnitudes of model melt rates by and large correspond to those observed for the major shelves, with stronger melting around the Amundsen Sea Embayment and the Peninsula. In the major Ross and Filchner-Ronne basins, although the model simulates some regions with freeze-on (blue shades), they are generally smaller in area and magnitude than in the observed maps.

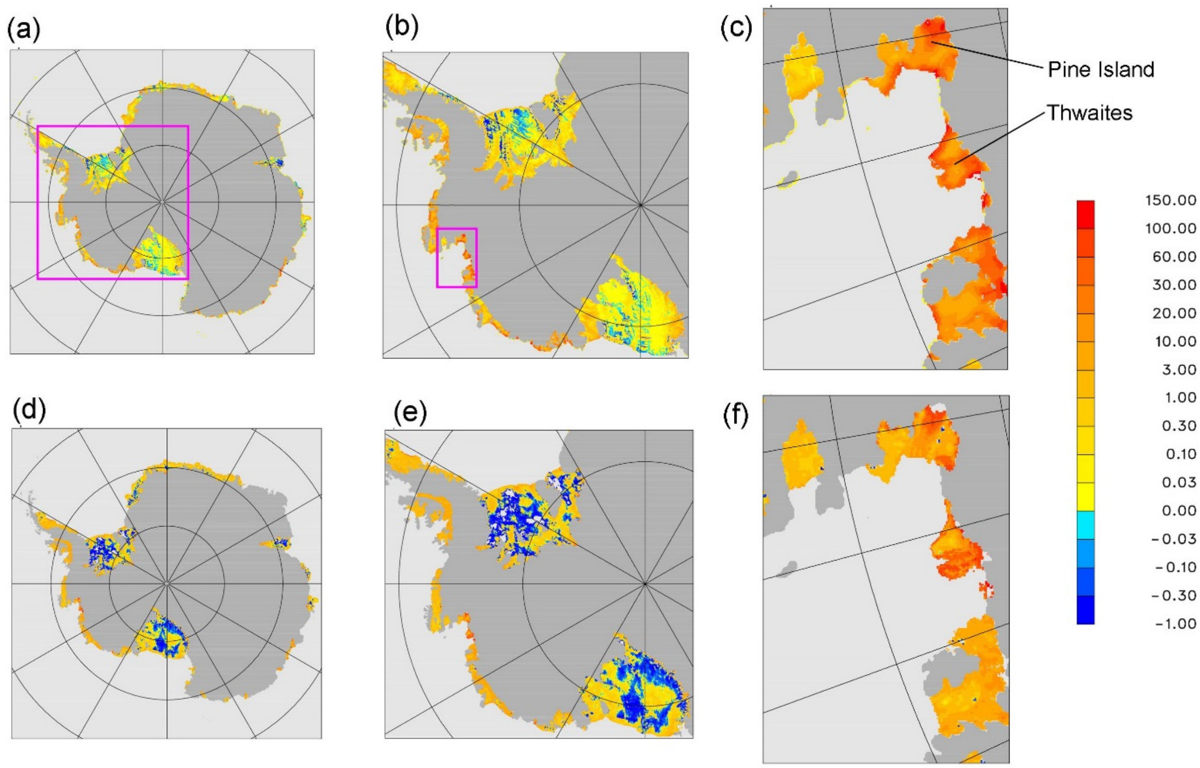

Figure 4. Maps of model and observed oceanic melt rates (m yr^{-1} of ice) below modern Antarctic ice shelves. **Upper row (a-c):** simulated using the two-layer balance-flux model. **Lower row (d-f):** observed, regridded from Adusumilli et al. (2020). **(a) and (d):** all Antarctica, 10 km grid. **(b) and (e):** West Antarctica, 5 km grid, magenta outline shown in panel a. **(c) and (f):** eastern Amundsen Sea Embayment, 2 km grid, magenta outline shown in panel b.

The same overall correspondence with the observed magnitudes is seen at finer scales and regions (center and right columns). The level of detail in the model results increases for finer resolutions, but there is little change in the overall patterns, indicating there is no strong spurious dependence on grid size in the model.

Within individual ice shelves, agreement with observed patterns is mixed. Correlation coefficients r in Table 1 are as high as ~0.6 (Pine Island, Stancomb-Brunt), but are lower for most shelves and as low as –0.25 for Totten. Similar levels of overall agreement and disagreement with observed melt-rate maps have been found in other modeling studies (Gwyther et al., 2014; Yokoyama et al., 2016; Lazeroms et al., 2018; Reese et al., 2018; Pelle et al. 2019, 2020). While some discrepancies are undoubtedly due to model shortcomings, uncertainties in the observations themselves may play a role, as discussed further below.

Following Reese et al. (2018), we compare melt rates averaged over individual ice shelves around Antarctica (Fig. 5 and Table 1). The bar chart in Fig. 5 also shows ice shelves using higher resolutions within the smaller domains of Fig. 4 (WAIS and ASE). As expected from the map results above, there is little difference in the shelf averages at different resolutions, although for most WAIS and ASE shelves there is a slight tendency towards higher melt rates at higher resolutions.

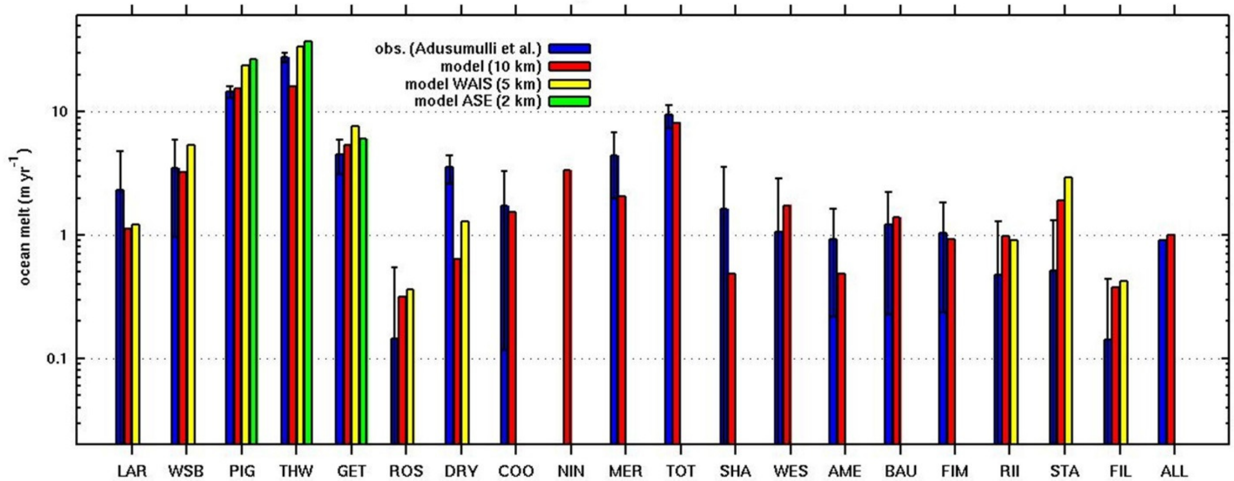

Figure 5. Average oceanic melt rates (m yr^{-1} of ice) for individual ice shelves (same set as in Reese et al., 2018; labels are defined in Table 1). Ice-shelf boundaries are determined by roughly estimated vertices of enclosing polygons. **Blue:** Observed, calculated from Adusumilli et al. (2020), 10 km grid. **Red:** Model, all shelves, 10 km grid. **Yellow:** Model, West Antarctic shelves, 5 km grid. **Green:** Model, Amundsen Sea Embayment shelves, 2 km grid.

Fig. 5 also includes observed averages calculated using the dataset of Adusumilli et al. (2020), aggregated from their 500-m grid to our 10 km model grid (these averages are generally very close to those in Adusumilli et al.'s Supplementary Table 1). There is reasonable agreement between model and observed for most shelves, especially for high-melt shelves such as Thwaites, Pine Island, Getz and Totten (THW, PIG, GET, TOT). There are larger discrepancies in the ratios for the larger Filchner-Ronne and Ross shelves (FIL, ROS), but the model does simulate the generally smaller magnitudes of these values correctly, and the absolute differences from observed are quite small (noting the logarithmic scale in Fig. 5).

	Ice shelf	area (km^2)	T_o (ºC)	S_o (PSU)	F_{uo} (Sv)	$\bar{m}$ (m yr^{-1})	$\bar{m}_{obs}$ (m yr^{-1})	$\bar{m}_{obs2}$ (m yr^{-1})	$\bar{m}$ -$\bar{m}_{obs}$ (m yr^{-1})	S	r
LAR	Larsen C	82077	-1.33	34.60	0.22	1.13	2.33±2.5	0.45±1.0	-1.20	2.16	-0.06
WSB	Wi.-St.-Ba.-Ge.	63549	1.17	34.67	0.17	3.23	3.46±2.5	1.46±1.0	-0.23	1.37	0.22
PIG	Pine Island	6940	0.46	34.55	0.11	15.47	14.49±1.6	16.20±1.0	0.98	1.08	0.63
THW	Thwaites	6940	0.46	34.55	0.18	15.94	27.63±2.4	17.73±1.0	-11.69	1.73	0.15
GET	Getz	43778	-0.37	34.41	0.33	5.41	4.49±1.4	4.26±0.4	0.92	1.25	0.18
ROS	Ross	506970	-1.58	34.63	0.50	0.32	0.15±0.4	0.10±0.1	0.17	2.70	0.24
DRY	Drygalski	4911	-1.84	34.78	0.03	0.64	3.53±0.9	3.27±0.5	-2.90	5.55	0.22
COO	Cook	4923	-1.62	34.58	0.04	1.54	1.72±1.6	1.33±1.0	-0.18	1.47	0.44

NIN	Ninnis	2162	-1.62	34.58	0.04	3.36		1.17±2.0			
MER	Mertz	5083	-1.62	34.58	0.04	2.06	4.40±2.4	1.43±0.6	-2.34	2.15	0.38
TOT	Totten	8764	-0.68	34.57	0.22	8.17	9.38±2.0	10.47±0.7	-1.21	1.16	-0.25
SHA	Shackleton	32592	-1.69	34.48	0.10	0.49	1.64±1.9	2.78±0.6	-1.15	3.58	0.27
WES	West	18703	-1.69	34.48	0.09	1.75	1.05±1.8	1.74±0.7	0.69	2.08	0.35
AME	Amery	64313	-1.72	34.53	0.25	0.48	0.92±1.7	0.58±0.4	-0.44	1.95	0.43
BAU	Baudouin	63651	-1.55	34.33	0.23	1.38	1.27±1.0	0.43±0.4	0.16	1.44	0.00
FIM	Fimbul	76866	-1.57	34.32	0.25	0.92	1.03±0.8	0.57±0.2	-0.11	1.40	0.45
RII	Riisen-Larsen	50514	-1.66	34.53	0.14	0.98	0.48±0.8	0.20±0.2	0.50	2.46	0.29
STA	Stancomb,Brunt	34716	-1.66	34.53	0.12	1.90	0.52±0.8	0.03±-.2	1.38	4.34	0.59
FIL	Filchner-Ronne	447756	-1.76	34.65	0.86	0.38	0.14±0.3	0.32±0.1	0.24	3.19	0.30
ALL	All above	1525209	-0.99	34.54	3.91	1.01	0.91	0.73	0.09	2.28	

Table 1. Model and observed ocean melt rates (m yr^{-1} of ice) and other quantities averaged over individual ice shelves (same set as in Reese et al. 2018; locations shown in Fig. 3). Ice-shelf extents are from Bedmachine (Morlighem, 2020; Morlighem et al., 2020), regridded to our 10-km polar stereographic grid. Individual ice-shelf boundaries are designated by roughly estimated vertices of surrounding polygons. **area** is total area resulting from our regridding and polygonal boundaries. $\boldsymbol{T_o}$ and $\boldsymbol{S_o}$ are ocean temperatures and salinities (PSU = ‰) obtained from WOA climatology (Boyer et al., 2018; see text), averaged around the ice-shelf edge and shifted uniformly for each shelf to match the averages in Reese et al. (2018, their Table 2; see text). $\boldsymbol{F_{uo}}$ is the total model mass flux from the upper-layer edge cells to the open ocean (Sv = 10^6 m^3 s^{-1}). $\bar{\dot{\boldsymbol{m}}}$ is model ocean melt, $\bar{\dot{\boldsymbol{m}}}_{\boldsymbol{obs}}$ is observed ocean melt calculated from regridded Adusumilli et al. (2020) data for 2010-2018, and $\bar{\dot{\boldsymbol{m}}}_{\boldsymbol{obs2}}$ is observed ocean melt reported in Reese et al. (2018) and Rignot et al. (2013) with data for several years to 2008, including uncertainty ranges reported in those papers. $\boldsymbol{S}$ is the score for each ice shelf given by Eq. (12). **r** is the correlation coefficient of $\dot{\boldsymbol{m}}$ vs. $\dot{\boldsymbol{m}}_{\boldsymbol{obs}}$ over individual grid cells for each ice shelf. **WSB** stands for Wilkins, Stange, Bach and George VI shelves. The smallest **Ninnis** shelf did not contain any Adusumilli et al. (2020) data when aggregated to our 10 km grid.

Table 1 includes observationally derived average melt rates both from Adusumilli et al. (2020) and Reese et al. (2013). Both sets are also shown in Fig. A2, along with whiskers showing the reported uncertainty ranges. There are significant differences between the two for some shelves, comparable to some of the differences from the model values. The reliability of observations (which are indirect, derived from satellite data on ice elevations and velocities and modeled surface mass balance) is not pursued further here, but may be a concern.

3.2 Modern ensemble

We performed an ensemble of model runs to explore parametric uncertainty in the model, varying four parameters, with five values for each given below.

- C_d = drag coefficient for upper-layer momentum (Eqs. 4b, 7). Ensemble values (non-dimensional) = .1, .3, 1, 3, 10 x 10^{-3}.
- Γ_T = parameter in the turbulent heat exchange coefficient $C_d^{1/2}\,\Gamma_T$ for upper-layer ice melting in Eqs. 4c and 5. Ensemble values (non-dimensional) = .1, .3, 1, 3, 10 x 10^{-2}.
- E_o = coefficient for the entrainment rate of lower-layer water into the upper layer (Eq. 2) Ensemble values (non-dimensional) = .1, .3, 1, 3, 6 x 10^{-2}.
- τ_α = duration of diffusive smoothing applied to sub-ice basal slopes sin α (Eq. 11). Ensemble values (years) = 0, .1, .3, 1 and 3, corresponding to length scales of effective smoothing $(D_d\,\tau_\alpha)^{1/2} \approx 0$, 3, 5, 10 and 17 km respectively.

The model was run for all combinations of values (625 runs), and a score was calculated for each run. Several different algorithms for scoring vs. observations were tried, aiming to provide meaningful validation across the wide range of shelf types (small to large area, low to high melt), and to allow for the reported uncertainty ranges in the observations. We used

$$S \;=\; \left[\left\{\; \max\left(\frac{\dot{m}_o}{\bar{\dot{m}}}\,,\frac{\bar{\dot{m}}}{\dot{m}_o}\right)\right\}\right] \qquad (12)$$

where $\bar{\dot{m}}$ is the model mean melt rate for an ice shelf. { } denotes an integral of the max ( ) quantity over a range of $\dot{m}_o$ values from $\bar{\dot{m}}_{obs}-3\sigma_{obs}$ to $\bar{\dot{m}}_{obs}+3\sigma_{obs}$, weighted assuming a normal probability distribution with mean $\bar{\dot{m}}_{obs}$ and standard deviation $\sigma_{obs} = \varepsilon_{obs}/1.96$. Here $\bar{\dot{m}}_{obs}$ is the observed ice-shelf mean calculated from the Adusumilli et al. (2020) data, and $\pm\varepsilon_{obs}$ is their reported 95% confidence interval (Table 1). Finally [ ] represents a simple average over all ice shelves in Table 1.

The use of ratios in (12) means neither low-melt nor high-melt shelves dominate in the [ ] average. The max quantity for an individual ice shelf is ≥ 1 and increases the more the model $\bar{\dot{m}}$ departs from $\dot{m}_o$ in either direction. However, the max quantity would become arbitrarily large if $\dot{m}_o$ approaches zero (i.e., if the magnitude of ε_{obs} is comparable to $\bar{\dot{m}}_{obs}$), so we restrict $\dot{m}_o$ values in (12) to ≥ 0.5 $\bar{\dot{m}}_{obs}$. The exact choice of this factor (~0.5) has no important effect on results.

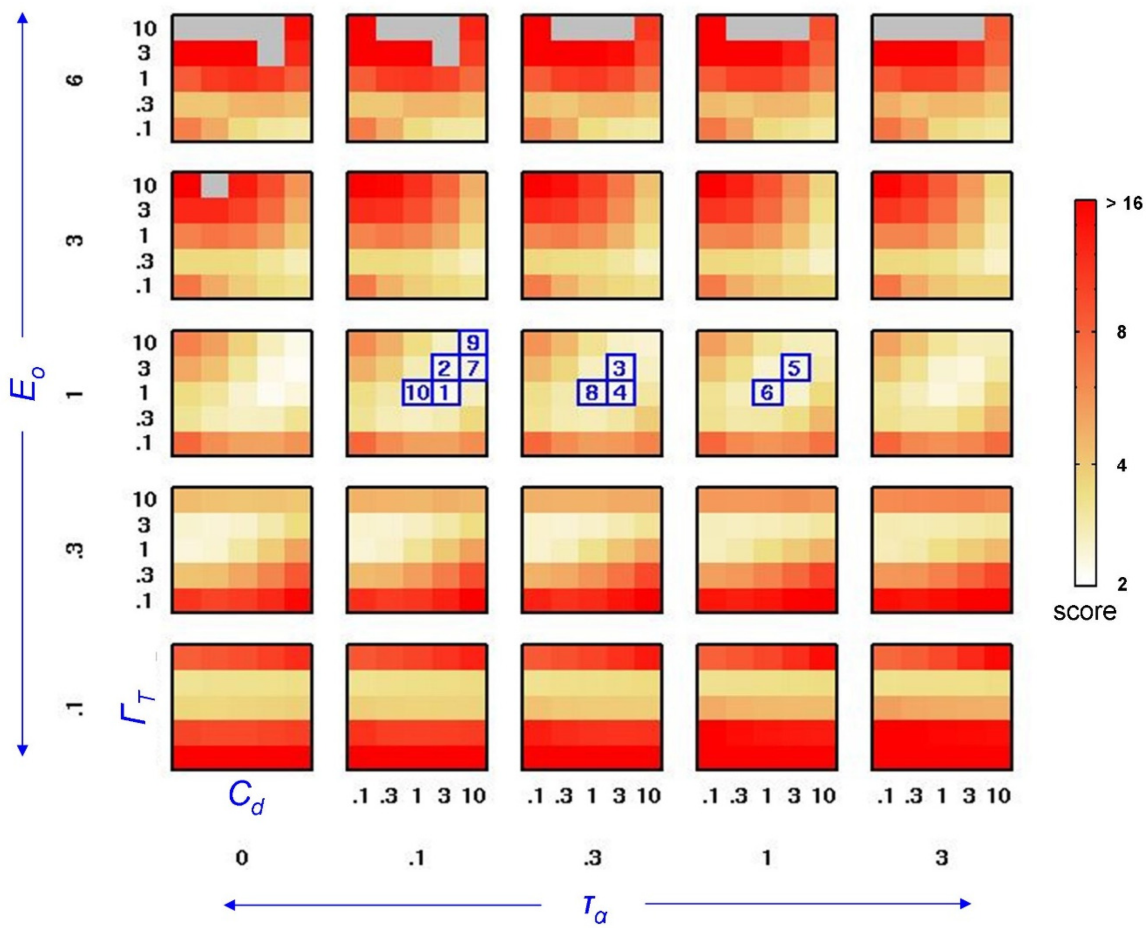

Figure 6. Scores in an ensemble of simulations for combinations of four parameters. The score in Eq. (12) measures departures from observed shelf-mean melt rates, ranging potentially from 1 (perfect fit) to ~16 and above (~no skill). The figure is organized to show the scores in the 4-D space of parameter variations, for parameters Cd, Γ_T, E_o and τ_α with 5 values each. Each small subpanel shows C_d (x axis) vs. Γ_T (y axis), and the subpanels are arranged bottom-to-top with increasing E_o, and left-to-right with increasing τ_α. Cd is the drag coefficient in Eqs. (1b) and (4b), with axis values x 10^{-3}. Γ_T enters in the heat exchange coefficient in Eqs. (1c) and (4c), with axis values x 10^{-2}. E_o is the entrainment coefficient in Eq. (2), with axis values x 10^{-2}. τ_α is the duration (years) that spatial diffusion is applied to smooth basal slopes sin α in Eq. (11). The combinations with the 10 best scores omitting the extreme values of τ_α (see text) are marked by blue numbered boxes, with scores ranging from 2.28 (#1) to 2.49 (#10). The poorest scores range up to ~60, but the color scale saturates for values >16 to better show the lower (more realistic) scores. Grey squares indicate runs that failed numerically due to drastically unrealistic melt rates, layer thicknesses and/or velocities; these occur only for extreme values of the parameters E_o and Γ_T, and their scores would be very poor.

The score S is shown for all members of the ensemble in Fig. 6. The duration of basal-ice-depth smoothing (τ_α, left-to-right subpanels) makes little difference in the scores. However flowline tests in SI section 5 for Pine Island Glacier shelf show that without any smoothing (τ_α = 0), small-scale fluctuations in basal ice depths cause considerable noise in the melt-rate results.

Reasonable results are obtained with some basal smoothing, but too much smoothing produces unrealistic close-to-linear basal profiles for durations of ~3 years or more (Fig. E2). Therefore we only consider scores for the three central columns of subpanels in Fig. 6 (τ_α = 0.1, 0.3 and 1 yr), and select the parameter combination with the best score (box # 1) for all model results shown in the paper, with $C_d = 3 \times 10^{-3}$, $\Gamma_T = 1 \times 10^{-2}$, $E_o = 1 \times 10^{-2}$, and $\tau_\alpha = 0.1$ years.

3.3 Different geometries than modern

As discussed above, the main motivation of this study is to enable melt rates to be calculated for general time-evolving land-sea geometries and ice shelves. In PICO and PICOP, individual ice-shelf basin outlines need to be designated over which transverse averaging is applied (Reese et al., their Fig. 3), and the model is applied separately for each basin.

During warm periods of the past, and potentially in the future, the bulk of West Antarctic marine ice is thought to have collapsed (e.g. Vaughan et al., 2011). If the central WAIS ungrounds and becomes ocean or ice shelf, the resulting configuration has no clear topological correspondence with the ice shelves and basins of today. We tried to develop an automatic algorithm that can sensibly define basin outlines for general grounding-line topologies, which could be used with PICO or PICOP, but were unable to find a method that works in full generality.

To show that the model here works for different geometries, it is applied here to two West Antarctic states from previous modeling. First, a snapshot from a future simulation (Pollard and DeConto, 2020) is used, 500 years into the future with atmospheric and oceanic forcing based on greenhouse-gas scenario RCP8.5 (without hydrofracturing or cliff failure), after which West Antarctica has partially collapsed. As seen in Fig. 7a, the model functions as intended, providing melt rates under the surviving ice shelves.

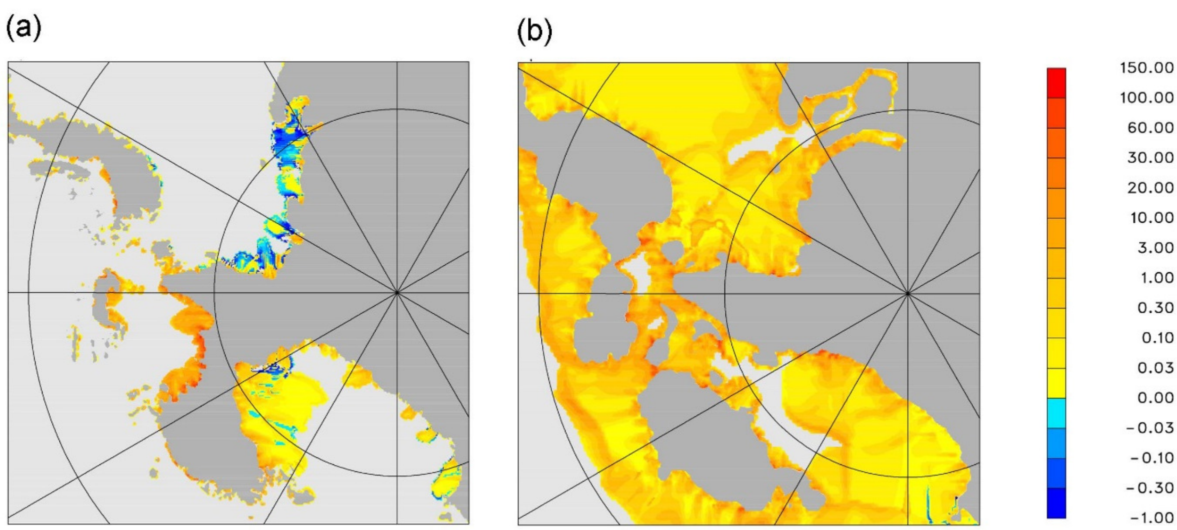

Figure 7. Modeled oceanic melt rates (m yr^{-1} of ice) for West Antarctic ice shelves with very different land-ocean-ice geometries than present. **(a)** Geometry from a future simulation with RCP8.5-like warming (Pollard and DeConto, 2020). **(b)** Geometry from a warm-Pliocene-like simulation after partial recovery due to subsequent climate cooling (Pollard et al., 2015). Light grey is open ocean, and darker grey is grounded ice or land.

Another snapshot is shown in Fig. 7b, during a period of regrowth of West Antarctica after a complete marine collapse, taken from a long-term simulation in Pollard et al. (2015, their Fig. S4D). In this simulation a nearly complete collapse of Antarctic marine-based ice has occurred due to warm mid-Pliocene-based atmospheric and oceanic warming, followed by ice regrowth towards modern conditions due to a return to a climate slightly cooler than today. The ice-sheet state in Fig 8b is 2000 years after the transition to the cooler climate, with grounding lines starting to re-advance into central West Antarctica. Again the model here functions as intended, producing reasonable melt rates under shelves with drastically different geometries than present.

For simplicity, the open-ocean temperatures and salinities used for the model in Fig. 8a,b are taken from the modern WOA 2018 dataset and extrapolated to the ice edges. In actual future or paleo applications, this forcing would be supplied by a dynamical ocean model running with the current land-ocean-ice geometries.

4. Summary and conclusions

A model of oceanic melting under ice shelves is described, simulating the basic two-layer overturning circulation of ocean water in the sub-ice cavity, with incoming flow from shelf edges to grounding lines in the lower layer, and reverse outgoing flow in the upper plume layer in contact with the ice base. The model is based on a series of similar models (LAZ/PICO/PICOP, in Lazerus et al., 2018; Reese et al., 2018; Pelle et al., 2019), and extends PICO and PICOP by using a balance-flux approach so that the model can be applied to general land-ocean-ice geometries without the need to pre-define individual basin boundaries.

Results are shown for modern Antarctic ice shelves, driven by climatological ocean temperature and salinity data (WOA, Boyer et al., 2018; Reese et al., 2018), and compared to modern melt rates derived mainly from satellite data of surface heights and ice velocities (Adusumilli et al, 2020; Reese et al., 2018). Results are presented for model resolutions ranging from 10 to 2 km, with no undue dependence on resolution found. An ensemble of model runs is performed, varying four of the more unconstrained model parameters, and using an overall score vs. observations for each model simulation to find the best-fit parameters. Fair agreement is achieved with the general magnitudes and average rates observed for individual ice shelves around Antarctica (following Reese et al., 2018), but the quality of intra-shelf patterns is mixed, in common with previous similar model studies (Gwyther et al., 2014; Yokoyama et al., 2016; Lazeroms et al., 2018; Reese et al., 2018; Pelle et al., 2019, 2020). Results from paleo and future model studies demonstrate that the model works as intended for geometries very different from the present.

The balance-flux model is computationally efficient enough to be used in long-term ice-sheet simulations. For continental Antarctica with a 10-km grid, one complete calculation takes 0.9 CPU seconds on a typical single processor, compared to 3.8 seconds per timestep (0.125 yr) for our ice-sheet model at the same resolution (e.g., DeConto and Pollard, 2016). However sub-ice-shelf melt does not need to be updated every timestep; if called once per model year, the CHICO component would take ~3 % of the CPU time of the whole model.

Further work will be aimed at improving agreement with observed melt distributions within individual ice shelves. Possible model extensions include exploring different distance metrics (SI section 2), adding subglacial water discharge as influx at grounding lines (Cai et al., 2017; Dow et al., 2020; Washam et al., 2020), and additional melting near ice-shelf edges due to warm-season Antarctic Surface Water (SI section 4). A more general question is whether two-layer thermohaline models can adequately capture cavity circulation seen in high-resolution dynamical ocean simulations (Dinniman et al., 2016; Asay-Davis et al., 2017; Richter et al., 2020), or at least the aspects that are important for sub-ice melt. For instance, are the oceanic quantities shown in SI section 3 reasonable, with return flows confined to a relatively thin ($\leq$ ~25 m) upper layer?

Acknowledgments

This work was supported by US National Science Foundation grant NSF ICER-1663693. Selected model output files, metadata and model code are available in the Penn State Data Commons archive at https://www.datacommons.psu.edu/commonswizard/MetadataDisplay.aspx?Dataset=6260

References

Adusumilli, S., Fricker, H.A., Medley, B., Padman, L., & Siegfried, M.. R.. (2020), Interannual variations in meltwater input to the Southern Ocean from Antarctic ice shelves. *Nature Geosc*., https://doi.org/10.1038/s41561-020-0616-z.

Alley, K. E., Scambos, T. A., Alley, R. B., & Holschuh, N. (2019), Troughs developed in ice-stream shear margins precondition ice shelves for ocean-driven breakup. *Sci. Adv*., 5, 10, eaax2215, doi: 10.1126/sciadv.aax2215.

Asay-Davis, X. S., Jourdain, N. C., & Nakayama, Y. (2017), Developments in simulating and parameterizing interactions between the Southern Ocean and the Antarctic Ice Sheet. *Curr. Clim. Change Rep.,* 3, 316–329, https://doi.org/10.1007/s40641-017-0071-0.

Boyer, T.P., Baranova, O. K., Coleman, C., Garcia, H. E., Grodsky, A., Locarnini, R. A., Mishonov, A. V., Paver, C. R., Reagan, J. R., Seidov, D., Smolyar, I. V., Weathers, K. W., & Zweng, M. M. (2018), *World Ocean Database 2018*, NCEI, NOAA Atlas NESDIS 87, https://www.nodc.noaa.gov/OC5/WOD/pr_wod.html.

Cai, C., Rignot, E., Menemenlis, D., & Nakayama, Y. (2017), Observations and modeling of ocean-induced melt beneath Petermann Glacier Ice Shelf in northwestern Greenland. *Geophys. Res. Lett.,* 44, 8396–8403,doi:10.1002/2017GL073711.

DeConto, R.M., & Pollard, D. (2016), Contribution of Antarctica to past and future sea-level rise. *Nature*, 531, 591-597.

Dinniman, M.S., Asay-Davis, X. S., Galton-Fenzi, B. K., Holland, P. R., Jenkins, A., & Timmermann, R. (2016), Modeling ice shelf/ocean interaction in Antarctica: A review. *Oceanography* 29(4):144-153, https://doi.org/10.5670/oceanog.2016.106.

Dow, C.F., McCormack, F. S., Young, D. A., Greenbaum, J. S., Roberts, J. L., & Blankenship, D. D. (2020), Totten Glacier subglacial hydrology determined from geophysics and modeling. *Earth Plan. Sci. Lett*., 531, https://doi.org/10.1016/j.epsl.2019.115961 (2020).

Dutrieux, P., De Rydt, J., Jenkins, A., Holland, P.R., Ha,, H.K., Lee, S.H., Steig, E.J., Ding, Q., Abrahamsen, E.P., Schroder, M. (2014). Strong sensitivity of Pine Island ice-shelf melting to climatic variability. *Science*, 343, 174-178.

Gwyther, D.E, Galton-Fenzi, B.K., Hunter, J.R., & Roberts, J.L. (2014), Simulated melt rates for the Totten and Dalton ice shelves. *Ocean Sci.,* 10, 267-279.

Hellmer, H. H., Kauker, F., Timmermann, R., Determann, J., & Rae, J. (2012), Twenty-first-century warming of a large Antarctic ice-shelf cavity by a redirected coastal current. *Nature*, 485, 225-228.

Holland, P. R., Jenkins, A., & Holland, D. M. (2008), The response of ice shelf basal melting to variations in ocean temperature, *J. Clim*., 21, 2558-2572.

Huang, P.-C., & Lee, K. T. (2015), A simple depression-filling method for raster and irregular elevation datasets. *J. Earth Syst. Sci*., 124, 1653-1685.

Jenkins, A. (1991), A one-dimensional model of ice shelf-ocean interaction. *J. Geophys. Res.-Oceans,* 96, 20671-20677.

Jenkins, A. (2011), Convection-driven melting near the grounding lines of ice shelves and tidewater glaciers. *J. Phys. Oceanogr*., 41, 2279-2294.

Jenkins, A., Shoosmith, D., Dutrieux, P., Jacobs S., Kim, T. W., Lee, S. H., Ha, H. K., & Stammerjohn, S. (2018), West Antarctic Ice Sheet retreat in the Amundsen Sea driven by decadal oceanic variability. *Nature Geosci*., 11, 733-738.

Lazeroms, W., Jenkins, A., Gudmundsson, H., & van de Wal, R. (2018), Modelling present-day basal melt rates for Antarctic ice shelves using a parametrization of buoyant meltwater plumes. *The Cryo*., 12,.49-70.

Miles, B. W. J., Jordan, J. R., Stokes, C. R., Jamieson, S. S. R., Gudmundsson, G. H., & Jenkins, A. (2020), Recent acceleration of Denman Glacier (1972-2017), East Antarctica, driven by grounding line retreat and changes in ice tongue configuration. *The Cryo. Disc*., https://doi.org/10.5194/tc-2020-162.

Moholdt, G., Padman, L., & Fricker, H. A. (2014), Basal mass budget of Ross and Filchner-Ronne ice shelves, Antarctica, derived from Lagrangian analysis of ICESat altimetry, *J. Geophys. Res.-Earth,* 119, 2361-2380, https://doi.org/10.1002/2014JF003171.

Morlighem, M. (2020). MEaSUREs BedMachine Antarctica, Version 2. Boulder, Colorado USA. *NASA National Snow and Ice Data Center Distributed Active Archive Center*. doi: https://doi.org/10.5067/E1QL9HFQ7A8M.

Morlighem, M., Rignot, E., Binder, T., Blankenship, D. D., Drews, R., Eagles, G., Eisen, O., Ferraccioli, F., Forsberg, R., Fretwell, P., Goel, V., Greenbaum, J. S., Gudmundsson, H., Guo, J., Helm, V., Hofstede, C., Howat, I., Humbert, A., Jokat, W., Karlsson, N. B., Lee, W., Matsuoka, K., Millan, R., Mouginot, J., Paden, J., Pattyn, F., Roberts, J. L., Rosier, S., Ruppel, A., Seroussi, H., Smith, E. C., Steinhage, D., Sun, B., van den Broeke, M. R., van Ommen, T., van Wessem, M., & Young, D. A. (2020), Deep glacial troughs and stabilizing ridges unveiled beneath the margins of the Antarctic ice sheet, *Nature Geoscience*, 13, 132-137. https://doi.org/10.1038/s41561-019-0510-8.

Olbers, D., &Hellmer, H. (2010), A box model of circulation and melting in ice shelf caverns. *Ocn. Dyn*., 60, 141-153.

Pelle, T., Morlighem, M., & Bondzio, J. H. (2019), Brief communication: PICOP, a new ocean melt parameterization under ice shelves combining PICO and a plume model. *The Cryo.,* 13, 1043-1049.

Pelle, T., Morlighem, M., & McCormack, F. S. (2020)., Aurora Basin, the Weak underbelly of East Antarctica. *Geophys. Res. Lett*., 47, e2019GL086821, https://doi.org/10.1029/2019GL086821.

Pollard, D., & DeConto, R. M. (2020), Improvements in one-dimensional grounding-line parameterizations in an ice-sheet model with lateral variations (PSUICE3D v2.1), *Geosci. Model Devel*., 13, 6481-6500, https://doi.org/10.5194/gmd-13-6481-2020.

Pollard, D., DeConto R. M., & Alley, R. B. (2015), Potential Antarctic Ice Sheet retreat driven by hydrofracturing and ice cliff failure. *Earth Plan. Sci. Lett*., 42, 112-121.

Reese, R., Albrecht, T., Mengel, M., Asay-Davis, X., & Winkelmann, R. (2018), Antarctic sub-shelf melt rates via PICO. *The Cryo*., 12, 1969-1985.

Richter, O., Gwyther, D. E., Galton-Fenzi, B. K., & Naughten, K. A. (2020), The Whole Antarctic Ocean Model (WAOM v1.0): Development and evaluation. *Geosci. Model Devel. Discuss.*, https://doi.org/10.5194/gmd-2020-164.

Rignot, E., Jacobs, S., Mouginot, J., & Scheuchl, B. (2013). Ice-shelf melting around Antarctica, *Science*, 341, 266-270.

Roberts, J., Galton-Fenzi, B. K., Paolo, F. S., Donnelly, C., Gwyther, D. E., Padman, L., Young, D., Warner, R., Greenbaum, J., Fricker, H. A., Payne, A. J., Cornford, S., Le Brocq, A., van Ommen, T., Blankenship D., & Siegert, M.J. (2018), Ocean forced variability of Totten Glacier mass loss. In: Siegert, M.J., Jamieson, S.S.R., & White, D.A. (eds), Exploration of Subsurface Antarctica: Uncovering Past Changes and Modern Processes. *Geological Society, London, Special Publications,* 461, 175-186.

Schmidtko, S., Heywood, K.J., Thompson, A.F., & Aoki, S. (2014), Multidecadal warming of Antarctic waters. *Science*, 346, 1227-1331.

Shean, D.E., Joughin, I.R., Dutrieux, P., Smith, B. E., & Berthier, E. (2019), Ice shelf basal melt rates from a high-resolution digital elevation model (DEM) record for Pine Island Glacier, Antarctica. The Cryo., 13, 2633-2656.

Stevens, C., Hulbe, C., Brewer, M., Stewart, C., Robinson, N., Ohneiser, C., & Jendersie, S. (2020), Ocean mixing and heat transport processes observed under the Ross Ice Shelf control its basal melting. *Proc. Nat. Acad. Sci*., 117, 16799-16804.

Tinto, K. J., Padman, L., Siddoway, C. S., Springer, S. R., Fricker, H. A., Das, I., Caratori Tontini, F., Porter, D. F., Frearson, N. P., Howard, S. L., Siegfried, M. R., Mosbeux, C., Becker, M. K., Bertinato, C., Boghosian, A., Brady, N., Burton, B. L., Chu, W., Cordero, S.I., Dhakal1, T., Dong, L., Gustafson, C. D., Keeshin, S., Locke, C., Lockett, A., O'Brien, G., Spergel, J. J., Starke, S. E., Tankersley, M., Wearing, M. G., & Bell, R. E. (2019), Ross Ice Shelf response to climate driven by the tectonic imprint on seafloor bathymetry. *Nature Geosc*., 12, 441-449.

Warner, R. C., & Budd, W. F. (2000), Derivation of ice thickness and bedrock topography in data-gap regions over Antarctica. *Ann. Glac*., 31, 191-197.

Washam, P., Nicholls, K. W., Muenchow, A, & Padman, L. (2020), Tidal modulation of buoyant flow and basal melt beneath Petermann Gletscher Ice Shelf, Greenland. *Geophys. Res.-Oceans*, 125, e2020JC016427. https://doi.org/10.1029/2020JC016427.

Yokoyama, Y., Anderson, J. B., Yamanea,, M., Simkins L. M., Miyairi, Y., Yamazaki, T., Koizumi, M., Suga, H., Kusahara, K., Prothro, L., Hasumia, H., Southon, J. R., & Ohkouchi, N. (2016), Widespread collapse of the Ross Ice Shelf during the late Holocene. *Proc. Nat. Acad. Sci*., www.pnas.org/cgi/doi/10.1073/pnas.1516908113.